

Bridging Synthetic-to-Real Gaps: Frequency-Aware Perturbation and Selection for Single-shot Multi-Parametric Mapping



Reconstruction

Linyu Fan, Che Wang, Ming Ye, Qizhi Yang, Zejun Wu, Xinghao Ding, Yue Huang,
Jianfeng Bao, Shuhui Cai, Congbo Cai

Abstract—Data-centric artificial intelligence (AI) has remarkably advanced medical imaging, with emerging methods using synthetic data to address data scarcity while introducing synthetic-to-real gaps. Unsupervised domain adaptation (UDA) shows promise in ground truth-scarce tasks, but its application in reconstruction remains underexplored. Although multiple overlapping-echo detachment (MOLED) achieves ultra-fast multi-parametric reconstruction, extending its application to various clinical scenarios, the quality suffers from deficiency in mitigating the domain gap, difficulty in maintaining structural integrity, and inadequacy in ensuring mapping accuracy. To resolve these issues, we proposed frequency-aware perturbation and selection (FPS), comprising Wasserstein distance-modulated frequency-aware perturbation (WDFP) and hierarchical frequency-aware selection network (HFSNet), which integrates frequency-aware adaptive selection (FAS), compact FAS (cFAS) and feature-aware architecture integration (FAI). Specifically, perturbation activates domain-invariant feature learning within uncertainty, while selection refines optimal solutions within perturbation, establishing a robust and closed-loop learning pathway. Extensive experiments on synthetic data, along with diverse real clinical cases from 5 healthy volunteers, 94 ischemic stroke patients, and 46 meningioma patients, demonstrate the superiority and clinical applicability of FPS. Furthermore, FPS is applied to diffusion tensor imaging (DTI), underscoring its versatility and potential for broader medical applications. The code is available at <https://github.com/flyannie/FPS>.

Index Terms—Unsupervised domain adaptation, reconstruction, perturbation, overlapping-echo detachment

I. INTRODUCTION

This work was supported in part by the National Key R&D Program of China under Grant 2022YFC2402102; and in part by the National Natural Science Foundation of China under Grant 12375291, 22161142024 and 82071913. (Corresponding author: Congbo Cai; Xinghao Ding.)

Linyu Fan, Che Wang, Ming Ye, Qizhi Yang, Zejun Wu, Shuhui Cai and Congbo Cai are with the Department of Electronic Science, Fujian Provincial Key Laboratory of Plasma and Magnetic Resonance, Xiamen University, Xiamen 361005, China (e-mail: flyannie@stu.xmu.edu.cn; w1873099961@163.com; yeming@stu.xmu.edu.cn; qzyang@stu.xmu.edu.cn; zejunwu@stu.xmu.edu.cn; shcai@stu.xmu.edu.cn; cbcai@xmu.edu.cn).

Xinghao Ding and Yue Huang are with the Key Laboratory of Multimedia Trusted Perception and Efficient Computing, Ministry of Education of China, Xiamen University, Xiamen 361005, China (e-mail: yhuang2010@xmu.edu.cn; dxh@xmu.edu.cn).

Jianfeng Bao is with the Department of Magnetic Resonance Imaging, The First Affiliated Hospital of Zhengzhou University, Zhengzhou University, Zhengzhou 450052, China (e-mail: baoguojianfeng@gmail.com).

ARTIFICIAL intelligence (AI) has fostered tremendous progress in medical imaging, including lesion segmentation, disease classification and reconstruction [1]. The full potential of data-driven AI remains constrained by medical data scarcity, with synthetic data emerging as a promising solution [2]–[4]. However, models trained on synthetic data often suffer performance degradation when applied to real-world scenarios, largely due to the persistent domain gaps, which poses a critical barrier to clinical translation. Consequently, bridging synthetic-to-real gaps represents a pivotal challenge in advancing medical image processing and analysis.

The lack of ground truth in real-world data further exacerbates the difficulty of bridging domain gaps. Although unsupervised domain adaptation (UDA) has realized notable progress in high-level medical tasks [5]–[7], its exploration in low-level tasks remains insufficient. Multi-parametric quantitative magnetic resonance imaging (mqMRI), as a crucial low-level task, has shown considerable potential in advancing objective clinical diagnostics [8]–[10] and in supporting numerous scientific research endeavors [11]. Moreover, mqMRI facilitates the definitive acquisition of diverse tissue properties, minimizing reliance on system conditions and human interpretation, meeting the increasing demands of precision medicine.

Estimating MR parameters is generally time-consuming, but techniques such as multiple overlapping-echo detachment (MOLED) [12] and multi-parametric MOLED [13] capture multiple MR echo signals with different signal evolutions in the same k -space, opening new avenues for accelerating mqMRI. Given its ultra-fast acquisition speed and exceptional resistance to motion artifacts, MOLED has been applied in various clinical scenarios, including the prediction of meningioma subtype [8], [9], the detection of stroke-related corticospinal tract change [10], the diagnosis of Huntington’s disease [14], and the transverse relaxation time (T_2) mapping of free-breathing abdominal [15]. Nonetheless, the reconstruction quality is still limited by the following constraints.

Deficiency in mitigating the domain gap. For mqMRI, the ground truth of real-world data is often inaccessible due to the complexity of physical parameter measurements and the irreversibility of physiological data acquisition. While synthetic data compensates for this limitation [16], synthetic-to-real gaps caused by non-ideal experimental factors, object variability and individual signal-to-noise ratios remain underexplored.

Employing UDA techniques to mitigate the domain gaps could maximize the value of both real-world data and synthetic data, enhancing model generalization and clinical applicability.

Difficulty in maintaining structural integrity. For clinical diagnosis, preserving fidelity and detail is essential. Existing methods often struggle with structural loss, excessive texture smoothing, and artifact generation. The generative adversarial network (GAN)-based approach for qMRI [17] suffers performance degradation in mqMRI due to the increasing complexity of adversarial interactions and the neglect of local detail modeling. Convolutional neural network (CNN)-based methods [13] lack global context and multi-scale learning, resulting in blurred edges and poor fidelity. Integrating Transformer-based global representation [18] with CNN-based multi-scale local detail preservation could enhance reconstruction reliability

Inadequacy in ensuring mapping accuracy. Homogeneous background regions in medical images, with minimal information content and straightforward mapping, often dominate the objective function during training [19], compromising reconstruction precision in regions of interest (ROIs). However, existing methods treat all regions equally, leading to inefficient computation and suboptimal reconstruction in meaningful areas [3], [13], [17]. Designing a frequency selection mechanism could prioritize informative components, enhancing sensitivity to ROIs and overall mapping accuracy.

To overcome aforementioned limitations, we proposed a novel frequency-aware perturbation and selection (FPS) approach for generalizable reconstruction. Built on the mean teacher architecture [20], FPS comprises two essential components: Wasserstein distance-modulated frequency-aware perturbation (WDFP) and hierarchical frequency-aware selection network (HFSNet). WDFP applies adaptive perturbations guided by the Wasserstein distance of the amplitude spectrum, promoting exploration of domain-invariant features. HFSNet, the backbone for both teacher and student models, incorporates feature-aware architecture integration (FAI), frequency-aware adaptive selection (FAS), and compact FAS (cFAS) within a multi-scale learning framework. Specifically, FAI seamlessly combines CNN, Swin Transformer (SwinT) [18] and multi-scale features to achieve multi-scale global-local information integration with optimal granularity. FAS dynamically generates frequency maps during decoupling, selectively emphasizing or attenuating frequency components before recalibration. Meanwhile, cFAS accomplishes frequency selection with expanded receptive fields in a more lightweight manner.

In the frequency domain, which holds substantial value for medical imaging, perturbation activates latent domain-invariant feature learning, while selection seeks optimal solutions within perturbation, establishing a robust and closed-loop learning pathway. This synergistic mechanism underpins the potential of FPS for broader medical fields. In summary, the main contributions of FPS can be summarized as fourfold.

- 1) To achieve more generalized reconstruction, we proposed the innovative FPS, which incorporates WDFP and HFSNet to bridge synthetic-to-real gaps.
- 2) To realize faithful structural fidelity, FAI was designed to facilitate multi-scale global-local interaction.
- 3) To advance reconstruction precision, FAS and cFAS

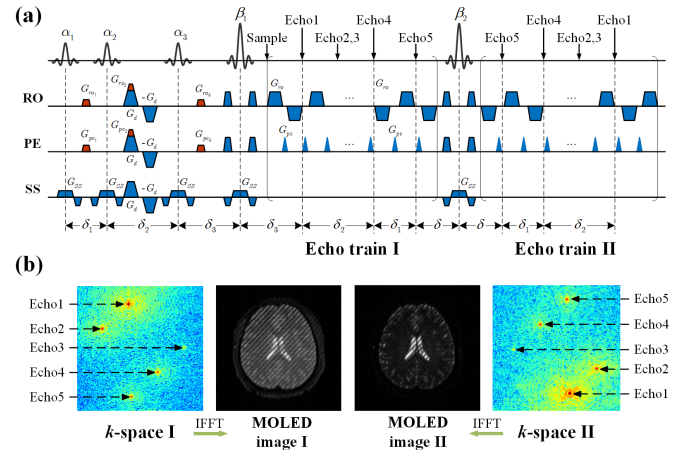


Fig. 1. (a) MOLED sequence. RO, PE and SS represent readout, phase-encoding and slice-selective directions; G_{ro}, G_{pe}, G_{ss} are corresponding gradients. α_1, α_2 and α_3 are excitation pulses with flip angles of 45° ; β_1 and β_2 are refocusing pulses with flip angles of 180° . G_{ro_z} and G_{pe_z} denote echo-shifting gradients; G_d denote bipolar diffusion gradients. δ_i ($i = 1, 2, 3$) denotes the interval between each excitation pulse. (b) Representative k -spaces and the corresponding MOLED images. FFT denotes the fast Fourier transform.

were developed to adaptively select the most informative frequency signals in an efficient manner.

- 4) Extensive experiments on synthetic data and diverse real clinical cases demonstrate the superiority, robustness and clinical applicability of our FPS.

II. RELATED WORKS

A. Multi-parametric quantitative MRI

Quantitative MRI is a valuable diagnostic tool that promotes biological tissue assessment through absolute physical quantities [21]. Current methods primarily focus on reconstructing multiple images from undersampled k -space data [22], which requires long acquisition times. OLED [23], MOLED [12] and multi-parametric MOLED [13] have introduced innovative strategies for accelerating MR parameter mapping, achieving real-time performance and high motion tolerance. MOLED adopted CNNs trained on synthetic data to achieve direct T_2 or effective transverse relaxation time (T_2^*) mapping, which may overlook domain gaps and lack the precision required to manage intricate physiological structures.

B. Unsupervised domain adaptation

UDA is a promising deep learning technology for reducing domain gaps without target domain annotations [24]. Various UDA strategies have been developed for medical applications, including explicit discrepancy minimization via discrepancy metrics [25], implicit discrepancy minimization via adversarial learning [26], image translation [27], disentangled representation learning [28], pseudo-labeling [29] and self-supervision [30]. Despite notable advancements achieved in high-level tasks such as classification [5], segmentation [6] and prediction [7], its application to low-level tasks [19] remains insufficient. The method [17], as an initial exploration in qMRI, is limited to single-parametric mapping. Due to the added complexity of the unstable adversarial process, it carries the risk of artifact interference and detail loss. Consequently, developing

a more advanced and versatile UDA framework is crucial for generalizable multi-parametric reconstruction.

III. METHODOLOGY

A. MOLED acquisition and reconstruction

The MOLED sequence, shown in Fig. 1(a), is described in previous research [13], enabling simultaneous mapping of apparent diffusion coefficient (*ADC*) and T_2 . Three excitation pulses are followed by two refocusing pulses to generate multiple signals. After each radiofrequency pulse, echo-shifting gradients are applied to introduce individual phase modulations in both readout and phase-encoding directions, thereby determining refocused positions of echoes in the k -space. As depicted in Fig. 1(b), although phase and magnitude differences among echo signals introduce interference stripes in MOLED images, the substantial information provided by these signals offers a reliable foundation for accurately estimating target parameters.

B. Frequency-aware perturbation and selection

The FPS architecture, illustrated in Fig. 2, is built on the mean teacher framework and comprises two key components: WDFP and HFSNet. The workflow of FPS involves inputting the real and imaginary parts of synthetic data S into the student model to generate $S_{T_2,ADC}$. Perturbed versions S' from WDFP are fed into the teacher model to produce $S'_{T_2,ADC}$. Supervised losses L_{sup} and L'_{sup} guide the outputs to match the ground truth $G_{T_2,ADC}$, while an unsupervised loss L_{un}^{syn} enhances consistency. Real-world data and perturbed data, R and R' , are processed to generate $R_{T_2,ADC}$ and $R'_{T_2,ADC}$, respectively. Without ground truth for real-world data, outputs are only constrained by the unsupervised loss L_{un}^{real} . Moreover, a multi-scale consistency constraint L_{con} is introduced, facilitating domain-invariant knowledge transfer across domains under varying degrees of perturbation.

The student network weights, θ_s , are updated via gradient descent to minimize L_{total} , while the teacher model weights, θ_t , are updated by exponential moving average (EMA):

$$L_{total} = L_{con} + L_{sup} + L'_{sup} + L_{un}^{syn} + \lambda_{real} \cdot L_{un}^{real}, \quad (1)$$

$$\theta_t = \alpha \theta_t + (1 - \alpha) \theta_s, \quad (2)$$

where $\lambda_{real} = e^{-5p^2}$, $p = 1 - iteration / (iteration_{total})$, and $\alpha = 1 - 1 / (iteration + 1)$ is a smoothing momentum.

1) **WDFP**: Given that k -space stores raw MRI data, its potential for bridging domain gaps has gained increasing recognition [31]. The phase component in k -space primarily encodes domain-invariant information, while the amplitude component, particularly in low-frequency regions, contains domain-variant information. Inspired by this, we proposed WDFP, which leverages adaptive perturbations to prioritize domain-invariant information learning.

For the $(i, j)_{th}$ frequency entry, k -space amplitude values of synthetic and real-world data, $\{K_{S_n}(i, j)\}_{n=1}^N$ and $\{K_{R_m}(i, j)\}_{m=1}^M$, are collected to calculate probabilistic distributions $P_S(i, j)$ and $P_R(i, j)$. The 1-Wasserstein distance $D(i, j)$ between $P_S(i, j)$ and $P_R(i, j)$ is computed. Wasserstein distance provides a stable and intuitive measure of domain distance, making it ideal for domain adaptation tasks

[32]. It enables the model to align relevant features across domains while minimizing the impact of irrelevant variations. The computed distance maps in Fig. 2 reveal larger distances at low-frequency points, consistent with the assumption that amplitudes of low-frequency components are primarily associated with domain-variant information.

To employ perturbations, the single-frequency activation $A(i, j)$ with a single non-zero element at (i, j) is defined, and the complex image $F(i, j)$ is derived by l^2 -normalized inverse fast Fourier transform (FFT) of $A(i, j)$ as

$$F(i, j) = \frac{\mathcal{I}FFT[A(i, j)]}{\|\mathcal{I}FFT[A(i, j)]\|_2}. \quad (3)$$

Then the perturbation $W(i, j)$ can be modulated based on the magnitude of domain distance $D(i, j)$,

$$W(i, j) = r \cdot \hat{D}(i, j) \cdot F(i, j), \quad (4)$$

where r is randomly sampled as either -1 or 1, and $\hat{D}(i, j) \in [0, 1]$ represents the normalized form of $D(i, j)$. Taking synthetic data as an example, the perturbed data is obtained by:

$$\text{Re}[S'] = \text{Re}[S] + \text{Re}[W(i, j)], \quad (5)$$

$$\text{Im}[S'] = \text{Im}[S] + \text{Im}[W(i, j)], \quad (6)$$

where $\text{Re}[\cdot]$ and $\text{Im}[\cdot]$ indicate the real and imaginary parts of a complex variable, respectively.

2) **HFSNet**: The input X_0 is fed into both the CNN and the SwinT, as illustrated in Fig. 3. SwinT extracts multi-level feature parameters, T_1 , T_2 , and T_3 , which capture diverse global relationships across three stages. Concurrently, CNN leverages UBlock and ResBlock to extract multi-level feature maps, M_1 , M_2 , and M_3 , capturing rich local details.

FAI. As shown in Fig. 3, FAI transforms SwinT feature parameters into feature-aware parameters β and γ through 3×3 convolutions. Subsequently, a regression-based merging technique combines CNN feature maps with β and γ . Low-resolution inputs, X_1 , X_2 , and X_3 , obtained via bilinear interpolation of X_0 , are concatenated to provide broader contextual information. The integrated feature maps are obtained by:

$$MI_s = \text{Concat}[X_s, (\beta_s \cdot M_s + \gamma_s)], \quad (7)$$

where s is the scale index. FAI aligns SwinT feature parameters with CNN feature maps, which captures robust spatial information from large-scale features and comprehensive semantic information from small-scale features.

FAS. The CNN feature maps are generated by the UBlock that optimizes shallow feature extraction and by the ResBlock. Both blocks comprise the same middle and final layers but differ in the deployment. FAS is utilized only in the final layer, while the simpler cFAS is applied in all layers. In Fig. 3, the input feature $X_{in} \in \mathbb{R}^{H \times W \times C}$ is first split into $x_i \in \mathbb{R}^{H \times W \times \frac{C}{b}}$, $i = 1, 2, \dots, b$, which are then processed through b branches with low-pass filters of varying kernel sizes $k \times k$. Each branch sequentially applies global average pooling (GAP), 1×1 convolution, batch normalization (BN), and the Softmax function to obtain the low-pass filter f_i^{low} . Then x_i is further divided into $x_i^{[j]} \in \mathbb{R}^{H \times W \times \frac{C}{b \times g}}$, $j = 1, 2, \dots, g$, and

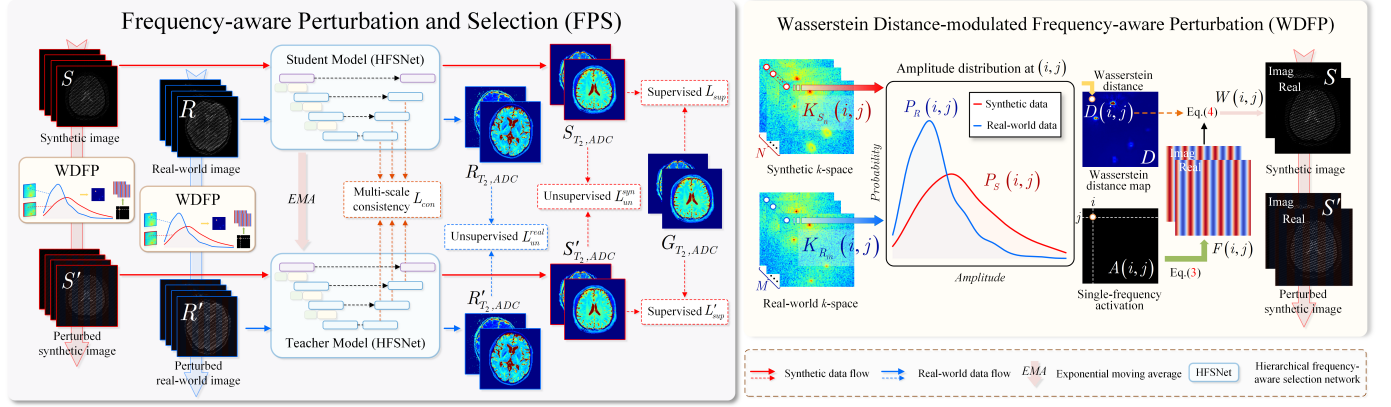


Fig. 2. Framework of FPS including two essential components, WDFP and HFSNet. The novel WDFP applies adaptive perturbation to synthetic and real-world data, facilitating domain-invariant feature learning, while HFSNet serves as the backbone for teacher and student models.

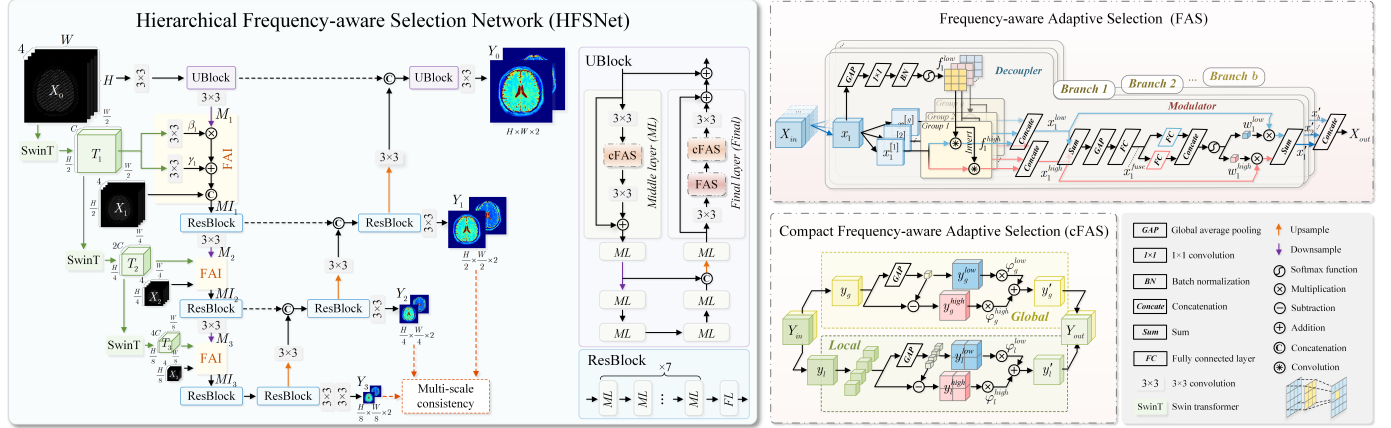


Fig. 3. Structure of HFSNet incorporates FAI, FAS and cFAS within a multi-scale learning framework. FAI seamlessly combines CNN, SwinT and multi-scale features. FAS comprises b branches, each containing filters of different kernel sizes. X_{in} is split, decoupled, modulated, and concatenated to produce X_{out} . cFAS consists of global and local branches. Y_{in} is divided into y_g and y_l , with y_l further partitioned into four windows. The low- and high-frequency components in each branch are rescaled and then combined to generate Y_{out} .

f_i^{low} is reshaped from $\mathbb{R}^{1 \times 1 \times gk^2}$ to $\mathbb{R}^{g \times k \times k}$. The corresponding high-pass filter f_i^{high} is derived by subtracting f_i^{low} from the identity kernel. Consequently, the low-frequency and high-frequency components, x_i^{low} and x_i^{high} , are extracted through:

$$x_i^{low}(h, w, c) = \sum_{p,q} f_i^{low}(p, q) x_i(h + p, w + q, c), \quad (8)$$

$$x_i^{high}(h, w, c) = \sum_{p,q} f_i^{high}(p, q) x_i(h + p, w + q, c), \quad (9)$$

where h and w denote the spatial coordinate, c is the channel index, and p and q are integers that range from $-\frac{k-1}{2}$ to $\frac{k-1}{2}$.

The FAS modulator starts with the feature fusion:

$$x_i^{fuse} = FC \left[GAP \left(x_i^{low} + x_i^{high} \right) \right], \quad (10)$$

where FC is a fully connected (FC) layer. Two additional FC layers are then utilized to generate attention weights w_i^{low} and w_i^{high} , and the output of each branch is then obtained by:

$$x'_i = w_i^{low} \cdot x_i^{low} + w_i^{high} \cdot x_i^{high}. \quad (11)$$

Ultimately, results from all branches $[x'_1, x'_2, \dots, x'_b]$ are concatenated to produce output X_{out} .

cFAS. Compared to FAS, cFAS employs two branches, as depicted in Fig. 3. Y_{in} is split into global and local parts, y_g and y_l , along the channel dimension. The global low-frequency component y_g^{low} is extracted via GAP, and the high-frequency component y_g^{high} is obtained by subtracting

y_g^{low} . To select significant frequency sub-bands, y_g^{low} and y_g^{high} are rescaled by learnable channel-wise weights ϕ_g^{low} and ϕ_g^{high} , which are optimized by backpropagation. In the local branch, $y_l \in \mathbb{R}^{H \times W \times C}$ is partitioned into four windows, each of size $\frac{H}{2} \times \frac{W}{2} \times \frac{C}{2}$. Similarly, the local low-frequency component y_l^{low} , corresponding high-frequency component y_l^{high} , and learnable weights ϕ_l^{low} and ϕ_l^{high} can be obtained. The updated global and local parts are

$$y'_g = \phi_g^{low} \cdot y_g^{low} + \phi_g^{high} \cdot y_g^{high}, \quad (12)$$

$$y'_l = \phi_l^{low} \cdot y_l^{low} + \phi_l^{high} \cdot y_l^{high}. \quad (13)$$

Finally, y'_g and y'_l are concatenated to produce the output Y_{out} .

3) Loss function: In MRI data, the frequency domain contains rich and valuable information. To fully exploit it, we incorporate spatial and frequency domain constraints:

$$\mathcal{SF}(x, y) = \|x - y\|_1 + \lambda \|\mathcal{FFT}(x) - \mathcal{FFT}(y)\|_1, \quad (14)$$

where λ is empirically set to 0.1. The L_{total} components are:

$$L_{con} = \sum_{s=1}^S [\mathcal{SF}(R_s, R'_s) + \mathcal{SF}(S_s, S'_s)], \quad (15)$$

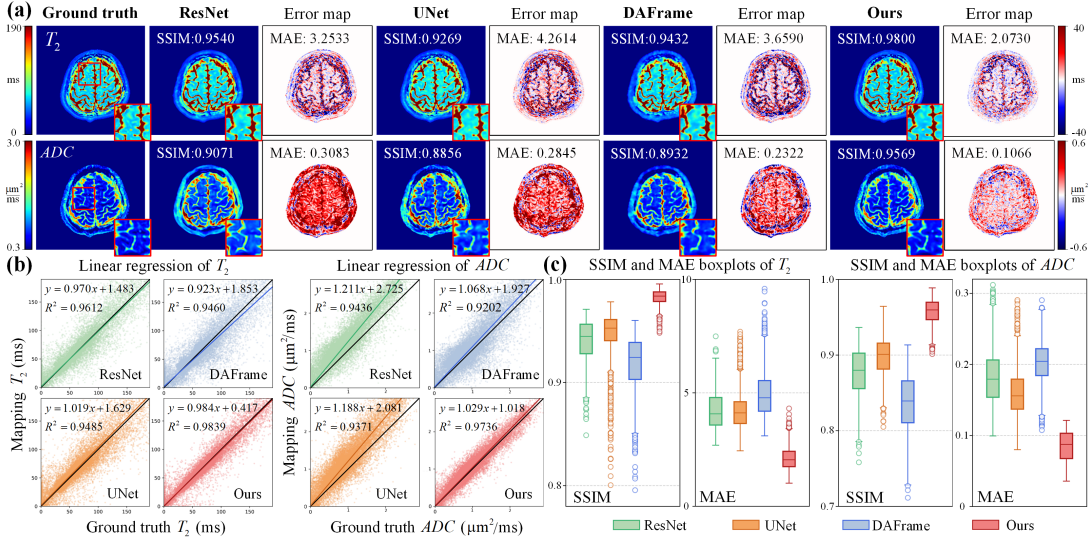


Fig. 4. Results of the numerical brain. (a) T_2 and ADC results and error maps of four methods. MAE was calculated within the display range of the colorbar. The zoomed-in views are displayed in the bottom-right corners. (b) Scatter plots of T_2 and ADC , which are shown along with the black identity lines, the linear regression lines of slopes, intercepts, and R^2 values. (c) Box plots of SSIM and MAE for T_2 and ADC on test data.

$$L_{sup} = \mathcal{S}\mathcal{F}(S_{T_2,ADC}, G_{T_2,ADC}), \quad (16)$$

$$L'_{sup} = \mathcal{S}\mathcal{F}(S'_{T_2,ADC}, G_{T_2,ADC}), \quad (17)$$

$$L_{un}^{syn} = \mathcal{S}\mathcal{F}(S_{T_2,ADC}, S'_{T_2,ADC}), \quad (18)$$

$$L_{un}^{real} = \mathcal{S}\mathcal{F}(R_{T_2,ADC}, R'_{T_2,ADC}), \quad (19)$$

where R_s and S_s represent the s -scale outputs from the student network for real-world and synthetic data, respectively, while R'_s and S'_s are outputs from the teacher network.

IV. EXPERIMENTS

A. Materials and data acquisitions

In this study, numerical brain data, along with human brain data from 5 healthy volunteers, 94 ischemic stroke patients, and 46 meningioma patients, were utilized. All data were acquired using a 3T MRI scanner (MAGNETOM Prisma, Siemens Healthcare, Germany). Approval for data acquisition was granted by the institutional research ethics committees, and informed consent was secured from the volunteers and patients. All MOLED images were obtained using the MOLED sequence with four diffusion directions, $\delta_1 = 11.90$ ms, $\delta_2 = 32.50$ ms, $\delta_3 = 11.88$ ms, in-plane acquisition matrix of 128×128 , field of view (FOV) of $220 \text{ mm} \times 220 \text{ mm}$, and b of $1000 \text{ s}/\text{mm}^2$. All reference scans were performed with the same FOV, acquisition matrix size and b .

1) *Synthetic training data*: The process for synthesizing training data is detailed in previous works [3]. To enhance generalization, abnormal templates constructed by overlaying lesion masks from a brain tumor dataset [33] were introduced to expand distributions. MR parameter values within these masks were then adjusted according to the range of reported stroke and tumor values [34]–[37]. A total of 10,000 pairs of synthetic data were used in the experiments, with 80% allocated for training and the remaining 20% used for validating.

2) *Data on healthy volunteers*: Reference T_2 maps were obtained using a spin-echo sequence with repetition time (TR) of 5.2 s, and four echo times (TEs) of 35 ms, 50 ms, 70 ms and

90 ms. Reference ADC maps were acquired using a single-shot echo-planar sequence with TR = 7.5 s, TE = 92 ms.

3) *Data on ischemic stroke patients*: Among the patients, 17 acute patients had an onset duration of 7 days or less, while 77 non-acute patients had an onset duration exceeding 7 days. Diffusion-weighted imaging (DWI) was performed to estimate reference ADC maps with TR of 4.6 s, and TE of 80 ms. T_2 –fluid-attenuated inversion recovery (FLAIR) images were performed with inversion time (TI) of 2.13 s, TR of 6.5 s, and TE of 85 ms. All images were registered to T_2 –FLAIR images and skull-stripped using FSL [38].

4) *Data on meningioma patients*: The 46 meningioma patients included 16 patients in the hard group and 30 patients in the soft group. T_2 –FLAIR images were performed with TI of 2.13 s, TR of 6.5 s, and TE of 85 ms.

B. Implementation details

We implemented FPS on Pytorch [39] with an NVIDIA GeForce RTX 3090 (24GB) and adopted Adamp [40] as the optimizer with the learning rate decreasing from $1e^{-4}$ to $1e^{-6}$. In the offline stage, the 1-Wasserstein distance maps in two k -spaces were computed. In the training stage, the batch size was set to 4, and the number of epochs was set to 200. ROIs used for statistical analysis were derived from several key brain regions, such as the thalamus, hippocampus, internal capsule, putamen, occipital lobe, and anterior white matter areas. Final ADC results were averaged across four diffusion directions.

C. Comparative algorithms

To evaluate the performance of FPS in mitigating the domain gap, we compared it with the domain adaptation framework (DAFrame) [17]. Meanwhile, to validate its reconstruction accuracy, we introduced the models based on ResNet [12] and UNet [13] as additional comparative algorithms. The parameter settings are consistent with the original papers.

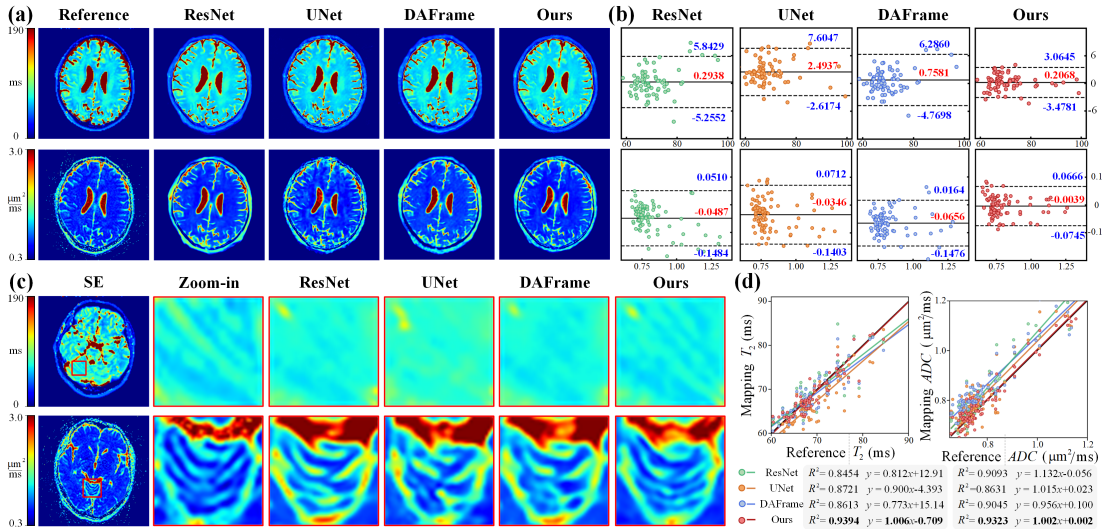


Fig. 5. Results of the healthy human brain. (a) Quantitative T_2 and ADC results comparison. (b) Bland-Altman analysis. (c) Zoomed T_2 and ADC maps. (d) Scatter plots of T_2 and ADC with the black identity lines, linear regression lines, slopes, intercepts, and R^2 values.

V. RESULTS

A. Results on numerical brain

The T_2 and ADC results of our FPS in Fig. 4(a) exhibit clear contrast in the gray matter, maintaining high accuracy, even in areas with higher values such as cerebrospinal fluid. In contrast, other methods suffer from structural blurring in the gray matter and abnormally high values. Furthermore, error maps provide an intuitive visualization, manifesting that FPS preserves structural details while effectively reducing errors, with a more uniform error distribution. From a quantitative evaluation perspective, FPS outperforms others with the best structural similarity index measure (SSIM) and mean absolute error (MAE), further confirming the superiority of our FPS.

In Fig. 4(b), the regression lines of FPS closely match the identity lines, along with superior R^2 values. The suboptimal ADC results observed in all methods underscore the greater challenges inherent in ADC mapping. Nonetheless, FPS effectively reconstructs ADC with minimal bias. In Fig. 4(c), FPS achieves a significantly higher median SSIM and a lower median MAE, indicating superior structural fidelity and enhanced reconstruction accuracy. Moreover, FPS demonstrates a narrower interquartile range and fewer outliers, further highlighting its consistent reliability and robustness.

B. Results on human brain data

1) *Healthy human brain analysis*: Visually, FPS achieves higher structural fidelity in the representative T_2 and ADC results presented in Fig. 5(a) and (c). ResNet, with limited attention to high-frequency information, produces overly smooth outputs with a loss of textural details. UNet, sensitive to input distributions, struggles to adapt from synthetic to real-world data, introducing artifacts and global inflated values. DAFrame, designed for single-parametric mapping, encounters greater challenges due to the increased complexity of adversarial interactions, leading to residual stripe artifacts and blurred textures. In contrast, FPS demonstrates robust domain adaptation, generating structurally accurate textures that closely match the reference without abnormal values.

Fig. 5(b) presents the Bland-Altman plots for 92 ROIs, with a narrower error distribution and fewer outliers FPS, indicating its superior robustness to extreme data. The average bias of FPS is closer to zero, reflecting better alignment with reference values. The linear regression lines of FPS in Fig. 5(d) reveal a slope near one and intercept near zero, with a significantly higher R^2 value and tighter alignment of scatter points, further confirming its stability and reliability.

2) *Ischemic stroke classification*: In ischemic stroke, T_2 changes provide valuable insights into tissue damage, onset timing and treatment decisions. T_2 maps generated by FPS in Fig. 6(a), along with the violin plots in Fig. 6(b), reveal varying degrees of T_2 increase in lesion areas. This aligns with studies [41], [42], which reported that T_2 values typically rise over time after ischemic stroke onset. These results evince that FPS, through precise reconstruction, is highly sensitive and reliable in detecting abnormal T_2 changes in brain tissue.

The variation in ADC is dynamic, influenced by the pathological mechanisms and temporal changes. Initially, ADC values decrease, followed by a potential increase in the non-acute phase [34], [42]. In Fig. 6(a), the ADC maps generated by FPS show clearer lesion boundaries and textures that better match the reference maps, offering more reliable information for subsequent classification. In contrast, other methods exhibit larger errors, struggling with domain discrepancies. Specifically, ResNet tends to overestimate ADC values with blurred textures and stripe artifacts around lesions, as seen in Patient D. UNet delineates the lesion areas well but introduces severe artifacts in normal brain tissues. Although DAFrame accurately localizes lesions, it produces higher ADC values in surrounding regions and is prone to striped interference. Fig. 6(b) presents the violin plots of our ADC results, where the variations between lesion and mirror regions, though subject to individual differences, fall within the expected range [42].

To validate the clinical applicability of methods, we performed ischemic stroke classification based on reconstructed maps. Histograms are constructed from T_2 and ADC values in lesion areas, and four histogram parameters are extracted:

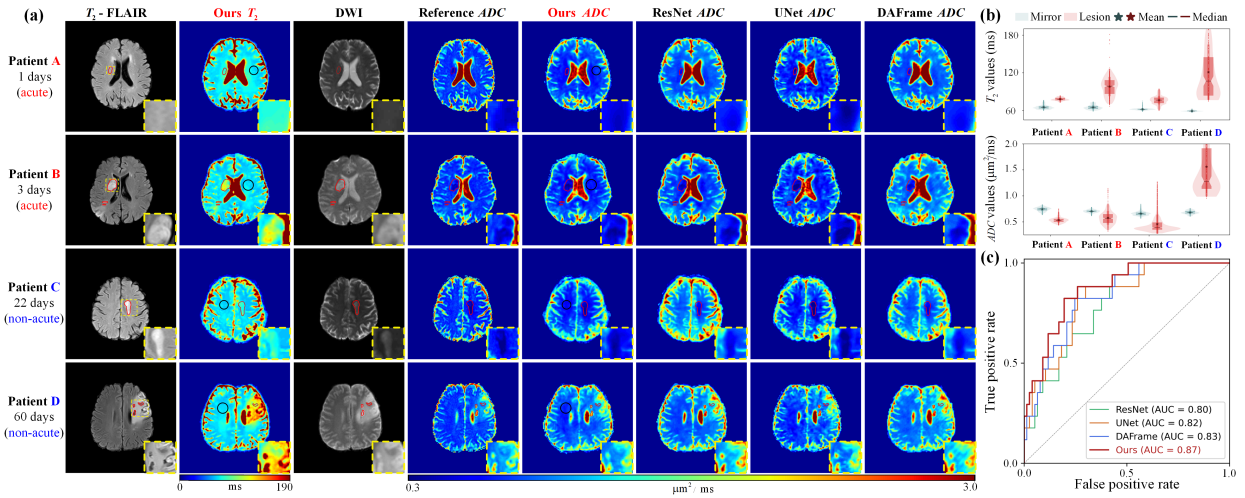


Fig. 6. Results of ischemic stroke patients. (a) Multi-modal reference images and results in four representative patients. Lesions are outlined in red, while mirror areas are marked with black circles. The zoomed-in views of the lesions, corresponding to the locations indicated by the yellow dashed lines, are shown in the bottom-right corner. (b) Violin plots of our T_2 and ADC results in lesion and mirror regions. (c) ROC curves of logistic regression for distinguishing 17 acute patients from 77 non-acute patients.

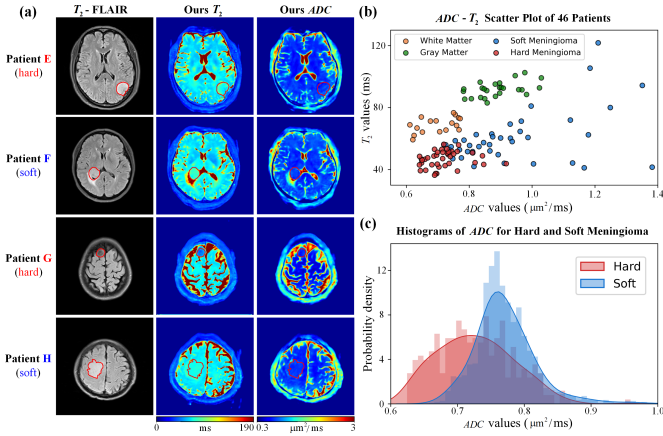


Fig. 7. Results of meningioma patients. (a) Multi-modal images in four representative patients. The meningioma lesions are delineated with red boundaries. (b) The $ADC - T_2$ scatter plot for our results in 46 meningioma patients. (c) Histograms of ADC in lesion regions for 16 hard meningioma patients and 30 soft meningioma patients.

the 75th percentile of T_2 , the 90th percentile of ADC , the median ADC , and ΔADC , which are then used in logistic regression to classify acute and non-acute patients [35], [43]. In Fig. 6(c), all of the comparison methods can perform the classification task effectively, but FPS achieves the highest area under the curve (AUC) and consistently outperforms the other methods during the rising phase of receiver operating characteristic (ROC) curves, demonstrating superior stability across different threshold settings. These results highlight the effectiveness of FPS in enhancing clinical decision-making, offering high accuracy, reliability, and adaptability to diverse clinical needs.

3) Meningioma consistency analysis: Meningioma is a common primary intracranial tumor. T_2 and ADC contribute valuable insights into its consistency evaluation, which is crucial for surgical planning and prognosis [44]. As shown in Fig. 7(a), results generated by FPS deliver clear and detailed texture information of lesion areas, closely resembling T_2 -FLAIR. Fig. 7(b) compares $ADC - T_2$ values across tissue types, including gray matter, white matter, and lesions from

soft and hard meningiomas. Gray and white matter clusters are tightly grouped, with values aligning with studies [45], [46], confirming the accuracy and stability of FPS in capturing normal tissue characteristics. In contrast, lesion areas exhibit greater dispersion, likely due to lesion progression, tissue type, and individual variability. However, these points remain within expected range [36], [37] and are clearly separated from gray and white matter. Additionally, soft and hard meningioma lesions show distinct distributions, underscoring the potential of FPS for reliable consistency assessment.

To evaluate the capability of FPS in predicting meningioma consistency, Fig. 7(c) illustrates histograms of our ADC results from lesion regions. The histograms reveal distinct ADC distributions between soft and hard meningiomas, with the values aligning with established clinical characteristics [36], [47]. These findings emphasize the effectiveness of FPS in providing clinically meaningful insights, refining meningioma feature quantification, as well as supporting tumor classification, treatment planning, and disease monitoring.

C. Ablation results

To investigate the benefits of components in FPS, an extensive ablation study was conducted using healthy brain data. Latent features were visualized using t-stochastic neighbor embedding (t-SNE) [48] in Fig. 8(a)-(c). In addition, T_2 and ADC results are exhibited in Fig. 8(d) and (e).

1) Effectiveness of WDFP in mitigating the domain gap: Two ablation methods are designed to validate the effectiveness of WDFP. The first, labeled w/o \mathcal{W} , removes WDFP and the mean teacher framework to assess the role of WDFP in promoting domain-invariant feature learning. The second, w/ \mathcal{N} , replaces WDFP with random Gaussian noise to evaluate the guiding role of Wasserstein distance. As shown in Fig. 8(a), omitting WDFP results in a clear distribution gap between synthetic and real-world data in the feature space. Furthermore, substituting WDFP with Gaussian noise, as depicted in Fig. 8(b), causes a wider scatter distribution. While noise slightly shifts the positions of real-world images (A, B, C)

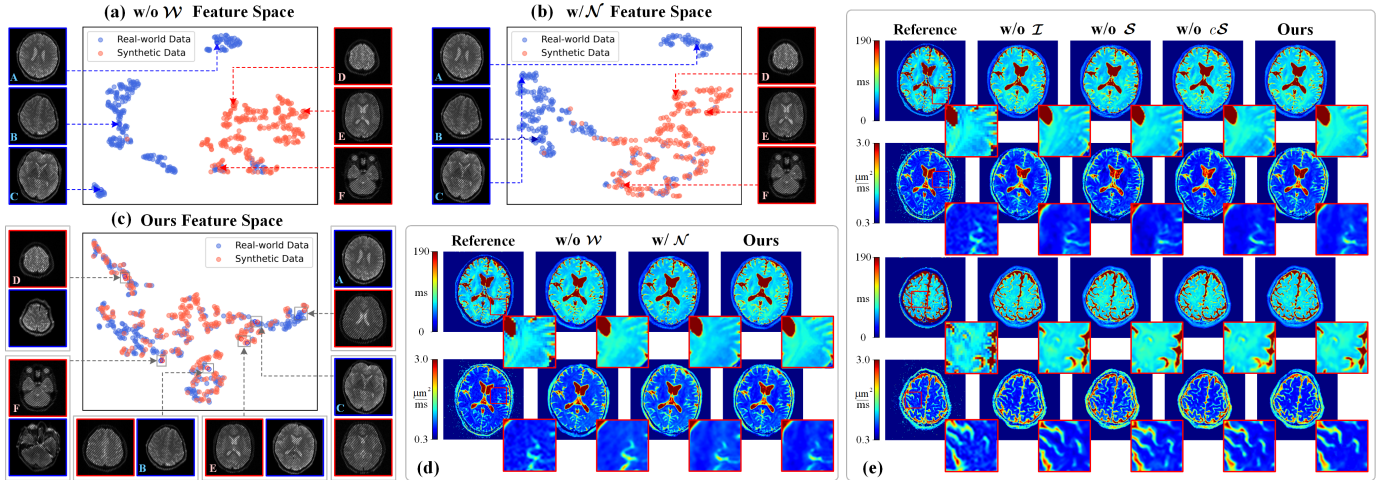


Fig. 8. Ablation results on healthy human brain. (a)-(c) T-SNE plots of feature vectors for synthetic and real-world data under different ablation methods. The MOLED images corresponding to representative points are also displayed around the T-SNE plots, with real-world images framed in blue and synthetic images framed in red. (d) (e) T_2 and ADC maps of ablation methods. The zoomed-in views are displayed in bottom-right areas.

and synthetic images (D, E, F), the feature distributions remain distinct, indicating that random noise alters distributions without addressing domain bias. Conversely, FPS fosters a stronger connection between synthetic and real-world data in Fig. 8(c). Corresponding images of real-world data points and their nearest synthetic data points exhibit similar structural features, showing effective domain-invariant feature learning.

Introducing Gaussian noise leads to global artifacts and lowers local values in the T_2 map, while ADC values are generally inflated, as displayed in Fig. 8(d). This noise introduces deviations, perturbing the relationship between inputs and outputs without reducing domain discrepancies. Furthermore, removing WDFP directly amplifies global stripe artifacts and causes localized ADC values to diverge from typical healthy brain tissue values. As a result, *w/o W* fails to learn domain-invariant features and mistakenly mixes lesion information from the training data into the real-world healthy brain data.

2) Effectiveness of HFSNet in enhancing mapping accuracy: To evaluate the contribution of each module in HFSNet, we implement three additional ablation methods. To begin with, we exclude FAI, thus removing global SwinT features and multi-scale information, denoted as *w/o I*. As illustrated in Fig. 8(e), the T_2 maps from *w/o I* display minor artifacts and lack texture details, whereas the ADC maps include values outside the normal tissue range. This indicates that removing FAI weakens the ability to capture contextual dependencies, resulting in a focus on local features and overlooking logical inconsistencies. To analyze the impact of frequency selection, subsequent experiments, *w/o S* and *w/o cS*, are conducted by removing FAS and cFAS, respectively. Both configurations generate T_2 maps with strip-like artifacts in the first row of Fig. 8(e) and blurred structure boundaries in the second row. For *w/o S*, ADC maps exhibit high-value artifacts and low-value shadows. These results reveal that omitting FAS impedes learning informative signals, thereby compromising reconstruction quality. In addition, removing cFAS disrupts the balance between global and local information, as well as high- and low-frequency components, leading to overly

smooth maps that fail to capture subtle textures.

3) Generalization verification of HFSNet in diffusion tensor imaging: To evaluate the robustness of HFSNet across reconstruction tasks, we applied it to diffusion tensor imaging (DTI), which is effective in detecting traumatic brain injury, multiple sclerosis, and major depressive disorder [49]. DWI quantifies water diffusion along diffusion gradient directions, with the diffusion tensor capturing tissue anisotropy. Eigenvalue decomposition of the tensor generates DTI parameter maps, including fractional anisotropy (FA), mean diffusivity (MD), axial diffusivity (AD), and radial diffusivity (RD). High-quality DTI typically requires multiple-direction DW images; however, we used only six directions to reduce scanning time and compared FPS with DIFFNet [50] and SuperDTI [51]. Data were obtained from the Human Connectome Project WU-Minn-Ox Consortium public database [52], approved by institutional ethics committees. We randomly selected 200 healthy participants, with 135 for training, 45 for validation, and 20 for testing. Fig. 9 presents qualitative and quantitative results, including peak signal-to-noise ratio (PSNR), SSIM, and normalized root mean squared error (NRMSE) [49]. HFSNet generated visualizations closest to the reference and achieved optimal values across all metrics. These results highlight the strong performance of HFSNet across different reconstruction tasks and underscore its potential for broader application in medical imaging.

VI. DISCUSSION

In this paper, the domain gap problem in the physics-guided synthetic data-driven training method is explored for multi-parametric quantitative MRI reconstruction. Compared with supervised training or physics-driven self-supervised training, the synthetic data-driven training method has two outstanding advantages: (1) it does not require a large number of labeled real training samples, which is particularly important for rapid quantitative MRI reconstruction, because of the scarcity of quantitative MRI data and the difficulty of obtaining real

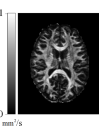

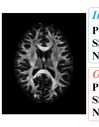

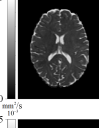

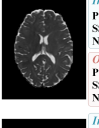
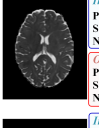
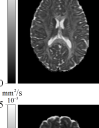
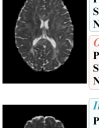

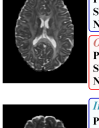
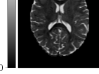
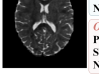
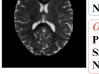
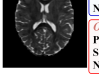
	Reference Visualization	DIFFNet Visualization	DIFFNet Metrics	SuperDTI Visualization	SuperDTI Metrics	Ours Visualization	Ours Metrics
FA			<i>Image-wise</i> PSNR: 20.3122 SSIM: 0.7778 NRMSE: 0.4150 <i>Overall</i> PSNR: 21.9678 SSIM: 0.7988 NRMSE: 0.5071		<i>Image-wise</i> PSNR: 27.8819 SSIM: 0.9182 NRMSE: 0.1736 <i>Overall</i> PSNR: 27.0860 SSIM: 0.9056 NRMSE: 0.3950		<i>Image-wise</i> PSNR: 28.7451 SSIM: 0.9266 NRMSE: 0.1572 <i>Overall</i> PSNR: 29.1568 SSIM: 0.9436 NRMSE: 0.2390
MD			<i>Image-wise</i> PSNR: 33.5468 SSIM: 0.9588 NRMSE: 0.0977 <i>Overall</i> PSNR: 34.4679 SSIM: 0.9696 NRMSE: 0.0858		<i>Image-wise</i> PSNR: 39.6971 SSIM: 0.9779 NRMSE: 0.0482 <i>Overall</i> PSNR: 38.8152 SSIM: 0.9712 NRMSE: 0.0945		<i>Image-wise</i> PSNR: 41.0572 SSIM: 0.9891 NRMSE: 0.0370 <i>Overall</i> PSNR: 39.3415 SSIM: 0.9871 NRMSE: 0.0821
AD			<i>Image-wise</i> PSNR: 32.0130 SSIM: 0.9357 NRMSE: 0.1529 <i>Overall</i> PSNR: 31.2066 SSIM: 0.9426 NRMSE: 0.1650		<i>Image-wise</i> PSNR: 37.3917 SSIM: 0.9723 NRMSE: 0.0586 <i>Overall</i> PSNR: 36.1220 SSIM: 0.9604 NRMSE: 0.1093		<i>Image-wise</i> PSNR: 38.2554 SSIM: 0.9847 NRMSE: 0.0531 <i>Overall</i> PSNR: 37.0163 SSIM: 0.9800 NRMSE: 0.0924
RD			<i>Image-wise</i> PSNR: 33.7206 SSIM: 0.9466 NRMSE: 0.1277 <i>Overall</i> PSNR: 33.6758 SSIM: 0.9620 NRMSE: 0.3760		<i>Image-wise</i> PSNR: 38.2967 SSIM: 0.9776 NRMSE: 0.0970 <i>Overall</i> PSNR: 37.9521 SSIM: 0.9754 NRMSE: 0.1572		<i>Image-wise</i> PSNR: 39.4524 SSIM: 0.9879 NRMSE: 0.0454 <i>Overall</i> PSNR: 38.4237 SSIM: 0.9853 NRMSE: 0.0937

Fig. 9. Qualitative and quantitative results of four parametric maps using diffusion weighted images with 6 diffusion gradient directions.

labels; (2) It avoids the need for explicit mathematical modeling of the signal, which is especially important for complex imaging sequences such as MOLED. Under a variety of non-ideal experimental factors, it is difficult to obtain the signal formula of MOLED accurately. Therefore, physics-guided synthetic data-driven deep learning techniques have gained significant applications in MR reconstruction, including MRI [53]–[55] and MR spectroscopy [4], [56], [57]. With the aid of these technologies, MOLED has achieved ultra-fast multi-parametric quantitative imaging [3], [12], [15], extending its application to various clinical scenarios [8]–[10], [14], [15]. However, while many important results have been achieved with synthetic data-driven techniques in the MR reconstruction field, bridging synthetic-to-real gaps remains an open issue. DAFrame still has many limitations as a pioneering approach to solving this important problem. The proposed FPS leverages perturbation to activate domain-invariant feature learning and utilizes selection to identify optimal solutions amidst instability, both within the frequency domain, which contains valuable information for medical imaging. This synergistic mechanism effectively mitigates the domain gap and enhances reconstruction quality, establishing a foundation for broader applications. This section discusses the clinical implications, innovations, strengths, limitations, and future research.

As shown in Fig. 4, FPS achieves exceptional reconstruction accuracy on data from the same distribution as the training set, attributed to the powerful performance of HFSNet. The advanced multi-scale global-local interaction capability of FAI ensures structural completeness, while the adaptive frequency selection in FAS and cFAS efficiently processes informative features, revealing finer texture details. For real-world data, FPS delivers high-fidelity results with precise structural details, meeting clinical demands, as exhibited in Fig. 5–7. These results underline the considerable potential of FPS in improving diagnostic precision and clinical assessments. Specifically, WDFP adapts to varying data distributions, presenting a favorable solution for bridging domain discrepancies and enabling accurate T_2 and ADC maps free of artifact interference.

FAI captures both macro-level lesion-surrounding relationships and subtle tissue variations, while FAS and cFAS enhance sensitivity to frequency components, facilitating the extraction of low-frequency features in large-scale structures and high-frequency details for lesion areas. These capabilities support clinicians in accurately localizing lesions and assessing tissue characteristics, improving diagnostic reliability and efficiency. Additionally, Fig. 8 highlight the synergistic contribution of all proposed components, effectively mitigating domain gaps and substantially boosts reconstruction performance. Moreover, the results in Fig. 9 demonstrate exceptional performance of HFSNet on the DTI task, further confirming its substantial potential for a broad range of medical reconstruction applications.

This paper explores the frequency domain and proposes several innovative components tailored to the characteristics of medical data. By calculating Wasserstein distances in the k -space and applying modulated frequency perturbations, WDFP effectively leverages prior knowledge to enhance domain-invariant feature learning. Frequency-aware selection mechanisms in FAS and cFAS aim to find stability amidst instability and seek optimality within perturbation, which optimizes feature extraction, alleviates computational burdens and enhances clinical applicability. Additionally, FAI facilitates multi-scale and global-local feature interactions, strengthening structural coherence in reconstructed results. Its hierarchical design integrates diverse prior knowledge, enhancing feature representation and model generalization. Collectively, these innovations improve reconstruction robustness and refinement while providing scalable, versatile, and flexible solutions for broader applications in medical image processing.

The proposed FPS demonstrates significant advantages by seamless integration of each module, effectively bridging synthetic-to-real gaps while ensuring both accuracy and stability across diverse experiments. Further work will continue to explore the feasibility and reliability of this approach in other application areas and to address more challenging scenarios, such as fat signal contamination, flow artifacts, multi-center datasets and high-resolution imaging.

VII. CONCLUSION

This article proposed an unsupervised domain adaptation framework, FPS, to address key challenges in multi-parametric mapping reconstruction, including deficiency in mitigating the domain gap, difficulty in maintaining structural integrity, and inadequacy in ensuring mapping accuracy. To bridge synthetic-to-real gaps, we integrated WDFP and HFSNet into the mean teacher framework. Additionally, we introduced FAI to facilitate multi-scale global-local interaction, realizing faithful structural fidelity. Furthermore, we designed FAS and cFAS, which adaptively select the most informative frequency signals, efficiently and comprehensively advancing reconstruction precision. The superior performance of FPS is demonstrated through comparative experiments on numerical brain, healthy human brain, real clinical cases, and the DTI task. Comprehensive ablation studies further highlight the individual contributions of the proposed components, which collectively enhance reconstruction refinement.

REFERENCES

- [1] X. Chen *et al.*, "Recent advances and clinical applications of deep learning in medical image analysis," *Med. Image Anal.*, vol. 79, p. 102444, 2022.
- [2] C. Gao *et al.*, "Synthetic data accelerates the development of generalizable learning-based algorithms for x-ray image analysis," *Nat. Mach. Intell.*, vol. 5, no. 3, pp. 294–308, 2023.
- [3] Q. Yang *et al.*, "Model-based synthetic data-driven learning (most-dl): Application in single-shot t2 mapping with severe head motion using overlapping-echo acquisition," *IEEE Trans. Med. Imaging*, vol. 41, no. 11, pp. 3167–3181, 2022.
- [4] B. Chen *et al.*, "Two-dimensional laplace nmr reconstruction through deep learning enhancement," *J. Am. Chem. Soc.*, vol. 146, no. 31, pp. 21 591–21 599, 2024.
- [5] C. Abbet *et al.*, "Self-rule to multi-adapt: Generalized multi-source feature learning using unsupervised domain adaptation for colorectal cancer tissue detection," *Med. Image Anal.*, vol. 79, p. 102473, 2022.
- [6] X. Sun, Z. Liu, S. Zheng, C. Lin, Z. Zhu, and Y. Zhao, "Attention-enhanced disentangled representation learning for unsupervised domain adaptation in cardiac segmentation," in *Proc. Int. Conf. Med. Image Comput. Comput.-Assist. Intervent. (MICCAI)*, 2022, pp. 745–754.
- [7] Y. Zhang *et al.*, "Unsupervised domain selective graph convolutional network for preoperative prediction of lymph node metastasis in gastric cancer," *Med. Image Anal.*, vol. 79, p. 102467, 2022.
- [8] Z. Li *et al.*, "Preoperative subtyping of who grade 1 meningiomas using a single-shot ultrafast mr t2 mapping," *J. Magn. Reson. Imaging*, vol. 60, no. 3, pp. 964–976, 2024.
- [9] Z. Li *et al.*, "Positive progesterone receptor expression in meningioma may increase the transverse relaxation: First prospective clinical trial using single-shot ultrafast t2 mapping," *Acad. Radiol.*, vol. 31, no. 1, pp. 187–198, 2024.
- [10] Y. Zhang *et al.*, "Anti-motion ultrafast t2 mapping technique for quantitative detection of the normal-appearing corticospinal tract changes in subacute-chronic stroke patients with distal lesions," *Acad. Radiol.*, vol. 31, no. 6, pp. 2488–2500, 2024.
- [11] A. Alkemade *et al.*, "A unified 3d map of microscopic architecture and mri of the human brain," *Sci. Adv.*, vol. 8, no. 17, p. eabj7892, 2022.
- [12] J. Zhang *et al.*, "Robust single-shot t2 mapping via multiple overlapping-echo acquisition and deep neural network," *IEEE Trans. Med. Imaging*, vol. 38, no. 8, pp. 1801–1811, 2019.
- [13] L. Ma *et al.*, "Single-shot multi-parametric mapping based on multiple overlapping-echo detachment (moled) imaging," *NeuroImage*, vol. 263, p. 119645, 2022.
- [14] F. Wu *et al.*, "Application of anti-motion ultra-fast quantitative mri in neurological disorder imaging: Insights from huntington's disease," *J. Magn. Reson. Imaging*, vol. n/a, no. n/a, 2025.
- [15] X. Lin *et al.*, "Free-breathing and instantaneous abdominal t2 mapping via single-shot multiple overlapping-echo acquisition and deep learning reconstruction," *Eur. Radiol.*, vol. 33, no. 7, pp. 4938–4948, 2023.
- [16] Q. Yang, Z. Wang, K. Guo, C. Cai, and X. Qu, "Physics-driven synthetic data learning for biomedical magnetic resonance: The imaging physics-based data synthesis paradigm for artificial intelligence," *IEEE Signal Process. Mag.*, vol. 40, no. 2, pp. 129–140, 2023.
- [17] C. Zhang *et al.*, "Towards better generalization using synthetic data: A domain adaptation framework for t2 mapping via multiple overlapping-echo acquisition," *IEEE Trans. Med. Imaging*, pp. 1–1., 2023.
- [18] Z. Liu *et al.*, "Swin transformer: Hierarchical vision transformer using shifted windows," in *Proc. IEEE/CVF Int. Conf. Comput. Vis. (ICCV)*, 2021, pp. 9992–10 002.
- [19] X. Liu *et al.*, "Attentive continuous generative self-training for unsupervised domain adaptive medical image translation," *Med. Image Anal.*, vol. 88, p. 102851, 2023.
- [20] A. Tarvainen and H. Valpola, "Mean teachers are better role models: Weight-averaged consistency targets improve semi-supervised deep learning results," in *Proc. Adv. Neural Inf. Process. Syst.*, 2017, p. 1195–1204.
- [21] H.-L. M. Cheng, N. Stikov, N. R. Ghugre, and G. A. Wright, "Practical medical applications of quantitative mr relaxometry," *J. Magn. Reson. Imaging*, vol. 36, no. 4, pp. 805–824, 2012.
- [22] F. Wang, Z. Dong, T. G. Reese, B. Rosen, L. L. Wald, and K. Setsompop, "3d echo planar time-resolved imaging (3d-epti) for ultrafast multi-parametric quantitative mri," *NeuroImage*, vol. 250, p. 118963, 2022.
- [23] C. Cai *et al.*, "Single-shot t2 mapping using overlapping-echo detachment planar imaging and a deep convolutional neural network," *Magn. Reson. Med.*, vol. 80, no. 5, pp. 2202–2214, 2018.
- [24] S. Kumari and P. Singh, "Deep learning for unsupervised domain adaptation in medical imaging: Recent advancements and future perspectives," *Comput. Biol. Med.*, vol. 170, p. 107912, 2024.
- [25] F. Wu and X. Zhuang, "Cf distance: A new domain discrepancy metric and application to explicit domain adaptation for cross-modality cardiac image segmentation," *IEEE Trans. Med. Imaging*, vol. 39, no. 12, pp. 4274–4285, 2020.
- [26] A. K. Susmelj *et al.*, "Signal domain adaptation network for limited-view optoacoustic tomography," *Med. Image Anal.*, vol. 91, p. 103012, 2024.
- [27] S. Chen *et al.*, "Segmentation-guided domain adaptation and data harmonization of multi-device retinal optical coherence tomography using cycle-consistent generative adversarial networks," *Comput. Biol. Med.*, vol. 159, p. 106595, 2023.
- [28] D. Mahapatra *et al.*, "Alfredo: Active learning with feature disentanglement and domain adaptation for medical image classification," *Med. Image Anal.*, vol. 97, p. 103261, 2024.
- [29] A. Mottaghi, A. Sharghi, S. Yeung, and O. Mohareri, "Adaptation of surgical activity recognition models across operating rooms," in *Proc. Int. Conf. Med. Image Comput. Comput.-Assist. Intervent. (MICCAI)*, 2022, pp. 530–540.
- [30] N. A. Koohbanani, B. Unnikrishnan, S. A. Khurram, P. Krishnaswamy, and N. Rajpoot, "Self-path: Self-supervision for classification of pathology images with limited annotations," *IEEE Trans. Med. Imaging*, vol. 40, no. 10, pp. 2845–2856, 2021.
- [31] Z. Xu, H. Gong, X. Wan, and H. Li, "Asc: Appearance and structure consistency for unsupervised domain adaptation in fetal brain mri segmentation," in *Proc. Int. Conf. Med. Image Comput. Comput.-Assist. Intervent. (MICCAI)*, 2023, pp. 325–335.
- [32] V. M. Panaretos and Y. Zemel, "Statistical aspects of wasserstein distances," *Annu. Rev. Stat. Appl.*, vol. 6, no. Volume 6, 2019, pp. 405–431, 2019.
- [33] J. Cheng *et al.*, "Enhanced performance of brain tumor classification via tumor region augmentation and partition," *PLOS ONE*, vol. 10, no. 10, pp. 1–13, 2015.
- [34] T. Kucinski *et al.*, "Correlation of apparent diffusion coefficient and computed tomography density in acute ischemic stroke," *Stroke*, vol. 33, no. 7, pp. 1786–1791, 2002.
- [35] S. Siemonsen *et al.*, "Quantitative t2 values predict time from symptom onset in acute stroke patients," *Stroke*, vol. 40, no. 5, pp. 1612–1616, 2009.
- [36] K. Miyoshi *et al.*, "Predicting the consistency of intracranial meningiomas using apparent diffusion coefficient maps derived from preoperative diffusion-weighted imaging," *J. Neurosurg.*, vol. 135, no. 3, pp. 969–976, 2021.
- [37] H. Yamada, M. Tanikawa, T. Sakata, N. Aihara, and M. Mase, "Usefulness of t2 relaxation time for quantitative prediction of meningioma consistency," *World Neurosurg.*, vol. 157, pp. e484–e491, 2022.
- [38] M. W. Woolrich *et al.*, "Bayesian analysis of neuroimaging data in fsl," *NeuroImage*, vol. 45, no. 1, Supplement 1, pp. S173–S186, 2009.
- [39] A. Paszke *et al.*, "Pytorch: An imperative style, high-performance deep learning library," in *Proc. Adv. Neural Inf. Process. Syst.*, 2019, pp. 8026–8037.
- [40] B. Heo *et al.*, "Adamp: Slowing down the slowdown for momentum optimizers on scale-invariant weights," *arXiv prepr. arXiv:2006.08217*, 2021.
- [41] R. A. Damion *et al.*, "Quantifying t2 relaxation time changes within lesions defined by apparent diffusion coefficient in grey and white matter in acute stroke patients," *Phys. Med. Biol.*, vol. 64, no. 9, p. 095016, 2019.
- [42] M. J. Knight *et al.*, "Determining t2 relaxation time and stroke onset relationship in ischaemic stroke within apparent diffusion coefficient-defined lesions. a user-independent method for quantifying the impact of stroke in the human brain," *Biomed. Spectrosc. Imaging*, vol. 8, no. 1–2, pp. 11–28, 2019.
- [43] G. Quan *et al.*, "Flair and adc image-based radiomics features as predictive biomarkers of unfavorable outcome in patients with acute ischemic stroke," *Front. Neurosci.*, vol. 15, 2021.
- [44] E. Fokkinga *et al.*, "Advanced diffusion-weighted mri for cancer microstructure assessment in body imaging, and its relationship with histology," *J. Magn. Reson. Imaging*, vol. 60, no. 4, pp. 1278–1304, 2024.
- [45] M. S. Bristow *et al.*, "Mr perfusion and diffusion in acute ischemic stroke: Human gray and white matter have different thresholds for infarction," *J. Cereb. Blood Flow Metab.*, vol. 25, no. 10, pp. 1280–1287, 2005.

- [46] R. Kumar, S. Delshad, M. A. Woo, P. M. Macey, and R. M. Harper, "Age-related regional brain t2-relaxation changes in healthy adults," *J. Magn. Reson. Imaging*, vol. 35, no. 2, pp. 300–308, 2012.
- [47] L. Zheng *et al.*, "Histogram analysis of mono-exponential, bi-exponential and stretched-exponential diffusion-weighted mr imaging in predicting consistency of meningiomas," *Cancer Imaging*, vol. 23, no. 1, p. 117, 2023.
- [48] J. Donahue *et al.*, "Decaf: A deep convolutional activation feature for generic visual recognition," in *Proc. Int. Conf. Mach. Learn. (ICML)*, 2014, p. I-647–I-655.
- [49] Z. Wu *et al.*, "Flexdti: flexible diffusion gradient encoding scheme-based highly efficient diffusion tensor imaging using deep learning," *Phys. Med. Biol.*, vol. 69, no. 11, p. 115012, 2024.
- [50] J. Park *et al.*, "Diffnet: Diffusion parameter mapping network generalized for input diffusion gradient schemes and b-value," *IEEE Trans. Med. Imaging*, vol. 41, no. 2, pp. 491–499, 2022.
- [51] H. Li *et al.*, "Superdti: Ultrafast dti and fiber tractography with deep learning," *Magn. Reson. Med.*, vol. 86, no. 6, pp. 3334–3347, 2021.
- [52] D. Van Essen *et al.*, "The human connectome project: A data acquisition perspective," *NeuroImage*, vol. 62, no. 4, pp. 2222–2231, 2012.
- [53] R. J. Chen, M. Y. Lu, T. Y. Chen, D. F. K. Williamson, and F. Mahmood, "Synthetic data in machine learning for medicine and healthcare," *Nat. Biomed. Eng.*, vol. 5, no. 6, pp. 493–497, 2021.
- [54] G. d. Maggiora *et al.*, "Deepspio: super paramagnetic iron oxide particle quantification using deep learning in magnetic resonance imaging," *IEEE Trans. Pattern Anal. Mach. Intell.*, vol. 44, no. 1, pp. 143–153, 2022.
- [55] J. Huang *et al.*, "Data- and physics-driven deep learning based reconstruction for fast mri: Fundamentals and methodologies," *IEEE Rev. Biomed. Eng.*, pp. 1–20, 2024.
- [56] X. Qu *et al.*, "Accelerated nuclear magnetic resonance spectroscopy with deep learning," *Angew. Chem. Int. Edit.*, vol. 59, no. 26, pp. 10297–10300, 2020.
- [57] H. Zhan, J. Liu, Q. Fang, X. Chen, Y. Ni, and L. Zhou, "Fast pure shift nmr spectroscopy using attention-assisted deep neural network," *Adv. Sci.*, vol. 11, no. 29, p. 2309810, 2024.